Facet tomography of chromia's magnetoelectric multipole

Paul Lehmann,[1] Kai Wagner,[1] Pavlo Makushko,[2] Oleksandr V. Pylypovskyi,[2,3] Igor Veremchuk,[2] Sophie F. Weber,[4] Nicola A. Spaldin,[5] Denys Makarov,[2] and Patrick Maletinsky[1]

[1]*Department of Physics, University of Basel, 4056 Basel, Switzerland*

[2]*Helmholtz-Zentrum Dresden-Rossendorf e.V., Institute of Ion Beam Physics and Materials Research, 01328 Dresden, Germany*

[3]*Department of Applied Physics and Nanomaterials, Kyiv Academic University, 03142 Kyiv, Ukraine*

[4]*Department of Physics and Astronomy, Chalmers University of Technology, SE-412 96 Gothenburg, Sweden*

[5]*Materials Theory, ETH Zürich, Wolfgang-Pauli-Strasse 27, 8093 Zürich, Switzerland*

(Received 9 January 2026; accepted 22 May 2026; published 4 August 2026)

Roughness-insensitive surface magnetization is an intrinsic property of magnetoelectric antiferromagnets and is today understood as a manifestation of bulk magnetoelectric multipoles. Here, we provide an experimental quantification of the crystal-facet-dependent surface magnetization in the archetypical magnetoelectric antiferromagnet Cr_2O_3 and show that the data are consistent with a quadrupolar component of the bulk magnetoelectric multipolization. Using quantitative nanoscale magnetometry on lithographically defined rectangular mesas that expose 30 distinct crystallographic facets, we quantify mesa stray magnetic fields, which arise from differences between the mesa top and side-facet magnetizations. The resulting dataset supports a linear map from surface normal to surface magnetization, from which we directly infer the bulk quadrupolar component within the multipolization framework. Our work provides systematic, facet-resolved evidence of roughness-insensitive surface magnetization, including in-plane components, and delivers a quantitative route to constraining bulk multipoles from surface stray-field data. Beyond addressing the modern theory of magnetoelectric multipolization, our approach offers a generally applicable method to quantify surface magnetizations in antiferromagnetic compounds and informs the choice of crystal cuts for future spintronics devices.

DOI: 10.1103/4l6w-pgdj

I. INTRODUCTION

In magnetoelectric materials, electric fields induce bulk magnetizations, and vice versa. Chromia (Cr_2O_3) was the first predicted [1] and experimentally confirmed [2–5] linear magnetoelectric (ME) antiferromagnet (AF), whose discovery and application potential have triggered an ongoing search for novel magnetoelectric AFs. This search is fueled by the advent of antiferromagnetic spintronics [6], where robustness to external fields and predicted high switching speeds [6–8] offer attractive prospects for novel memory architectures [9–14] that surpass the possibilities of ferromagnet-based devices. In this context, linear magnetoelectric AFs enable direct and efficient electrical manipulation of the AF order parameter [15], which is challenging otherwise.

Magnetoelectric AFs also exhibit an intrinsic, roughness-insensitive surface magnetization [16–18] that provides a defect-robust equilibrium moment that can be used to read the bulk order parameter. Building on the analogy with bound surface charges in ferroelectrics that result from bulk ferroelectric polarization, recent theoretical models explain the surface magnetization in linear magnetoelectrics as a manifestation of the bulk magnetoelectric multipolization [17]. The ME-multipolization quantifies the bulk spin structure asymmetry that in combination with the symmetry reduction by a surface leads to a roughness-insensitive surface magnetization [18,19]. Because these theoretical frameworks remain largely untested experimentally, a systematic study of the crystal-cut dependence of the surface magnetization in a magnetoelectric AF, such as Cr_2O_3, is crucial for establishing the magnetoelectric bulk-boundary correspondence and its implications for AF spintronics.

In Cr_2O_3, the surface magnetization has been studied extensively on the (001) plane, with recent extensions to (100) and ($\bar{1}20$) planes [18,20,21], using techniques including magnetometry [22–24], force microscopy [25], magnetic circular dichroism [20,26], magnetotransport [11,21,27], and exchange bias [15]. However, a systematic study of the crystal-cut dependence that would enable a comprehensive understanding of Cr_2O_3's surface magnetization is still missing.

Here, we employ scanning nitrogen-vacancy magnetometry (SNVM), a nanoscale magnetic-field imaging technique [28], to quantify field-generating surface magnetizations of Cr_2O_3 in a facet-resolved way across two single-crystal samples. Our experiments reveal a smooth dependence of surface magnetization on the surface normal and provide evidence for a roughness-insensitive surface magnetization on all facets of Cr_2O_3. Our analysis of the measured surface magnetization reveals that it is well described as a linear

Published by the American Physical Society under the terms of the Creative Commons Attribution 4.0 International license. Further distribution of this work must maintain attribution to the author(s) and the published article's title, journal citation, and DOI.

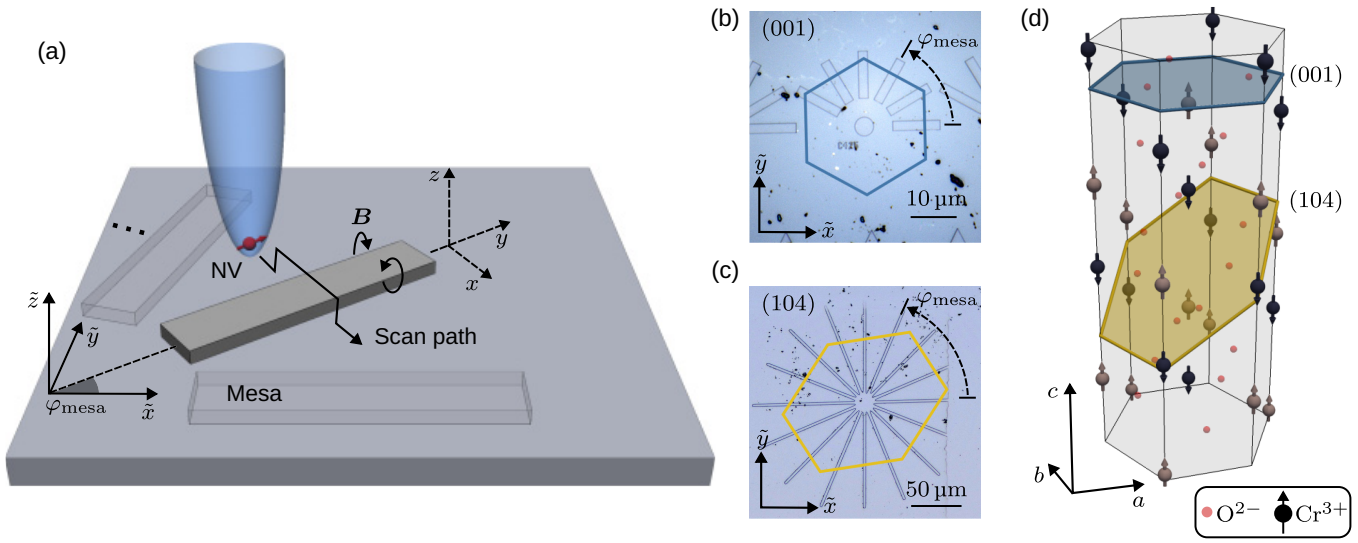


FIG. 1. Schematic illustration of the experiment and the studied Cr_2O_3 crystals. (a) Geometry of the scanning NV magnetometry (SNVM) measurement. Mesas with varying orientation were etched into a single crystal Cr_2O_3 substrate. The mesa's orientation is given by the angle φ_{mesa} between the mesa's long axis and the x axis of a global coordinate system aligned with the macroscopic sample shape. Stray magnetic fields are measured by SNVM along a line perpendicular to the mesa's long axis. (b), (c) Optical micrographs of mesas on the (001)- and (104)-oriented Cr_2O_3 crystals, respectively. (d) Hexagonal unit cell of Cr_2O_3's crystal structure showing the antiferromagnetic spin arrangement (arrows) along [001]. The spheres show positions of individual Cr ions. The (001)- and (104)-surface planes, which enclose an angle ≈38.5°, are indicated.

function of the surface normal. The fitted linear relationship is consistent across the two samples, despite their distinct sets of facets, corroborating a strong link between bulk symmetry and roughness-insensitive surface magnetization in magnetoelectric AFs. Our systematic study thereby establishes a link between surface magnetization and bulk multipole components that is readily extendable to other related compounds.

II. EXPERIMENTAL SETUP

The principle underlying our experiment is illustrated in Fig. 1(a). We measured the stray fields emerging from lithographically defined mesas using a scanning NV magnetometer (see Appendix C). The mesas serve as well-defined, controlled sources of stray field emerging from the surface magnetization, whereas the surface magnetization on an unstructured, monodomain sample would not produce any stray field. To obtain field profiles, we scanned along paths perpendicular to each mesa's long axis [see scan path in Fig. 1(a)]. Since both the top and the side facets of the mesas can carry surface magnetizations, the measured stray fields arise from the combination of both, as detailed below. Furthermore, since the mesas are lithographically defined, their orientation relative to crystallographic axes [characterized by angle φ_{mesa}, see Fig. 1(a)] can be readily controlled, thereby enabling measurements on many distinct crystal facets of Cr_2O_3. Optical images of representative mesa arrangements are shown in Figs. 1(b) and 1(c). To extend the accessible set of facets, we investigated two samples with different top facets, one with a (001)-oriented top surface and another with a (104)-oriented top surface, where (hkl) are Miller indices in the hexagonal unit cell. The relative orientations of the sample top facets to the hexagonal unit cell are illustrated in Fig. 1(d). Because the facet sets differ between the two samples, our measurements probe the surface magnetization of 30 facets in total—13 on the (001)-oriented sample and 17 on the (104)-oriented sample.

To obtain quantitative estimates of surface magnetization from the measured magnetic fields, we use an analytical model for the stray field linecuts across the mesas. For each mesa, we define a local coordinate system [see Fig. 1(a)] with x along the scan direction, z the sample normal, and y such that the coordinate system is right handed. We then model the mesa as a topographic step in the xz plane [Fig. 2(a)] that extends infinitely in y. We assign a homogeneous surface magnetization to the side and top facets, but allow the direction and strength of top- and side-facet magnetization to vary and take different, independent values. Due to the combined time-reversal and space-inversion symmetry of Cr_2O_3, the magnetizations on two opposing side facets are related by time inversion [Fig. 2(a)] [15,16,29].

To calculate the mesa stray field, we replace the magnetization by equivalent magnetic charges or currents [30]. Following Andreev [31], in-plane magnetization components orthogonal to mesa edges are represented by linear magnetic charge densities on the edges, and the out-of-plane magnetization components by edge currents. The linear magnetic charge density λ_M then equals the difference of in-plane magnetization components $\Delta m_{\parallel}$ across adjoining facets and the current I_M equals the difference of out-of-plane magnetization components $\Delta m_{\perp}$ [32]. For the top right edge [edge 3 in Fig. 2(a)], this yields

$$\lambda_M = m_x^{(23)} + m_z^{(34)}, \tag{1}$$

$$I_M = m_z^{(23)} - m_x^{(34)}, \tag{2}$$

where subscripts indicate the magnetization component and superscripts the corners of the respective facets as labeled in

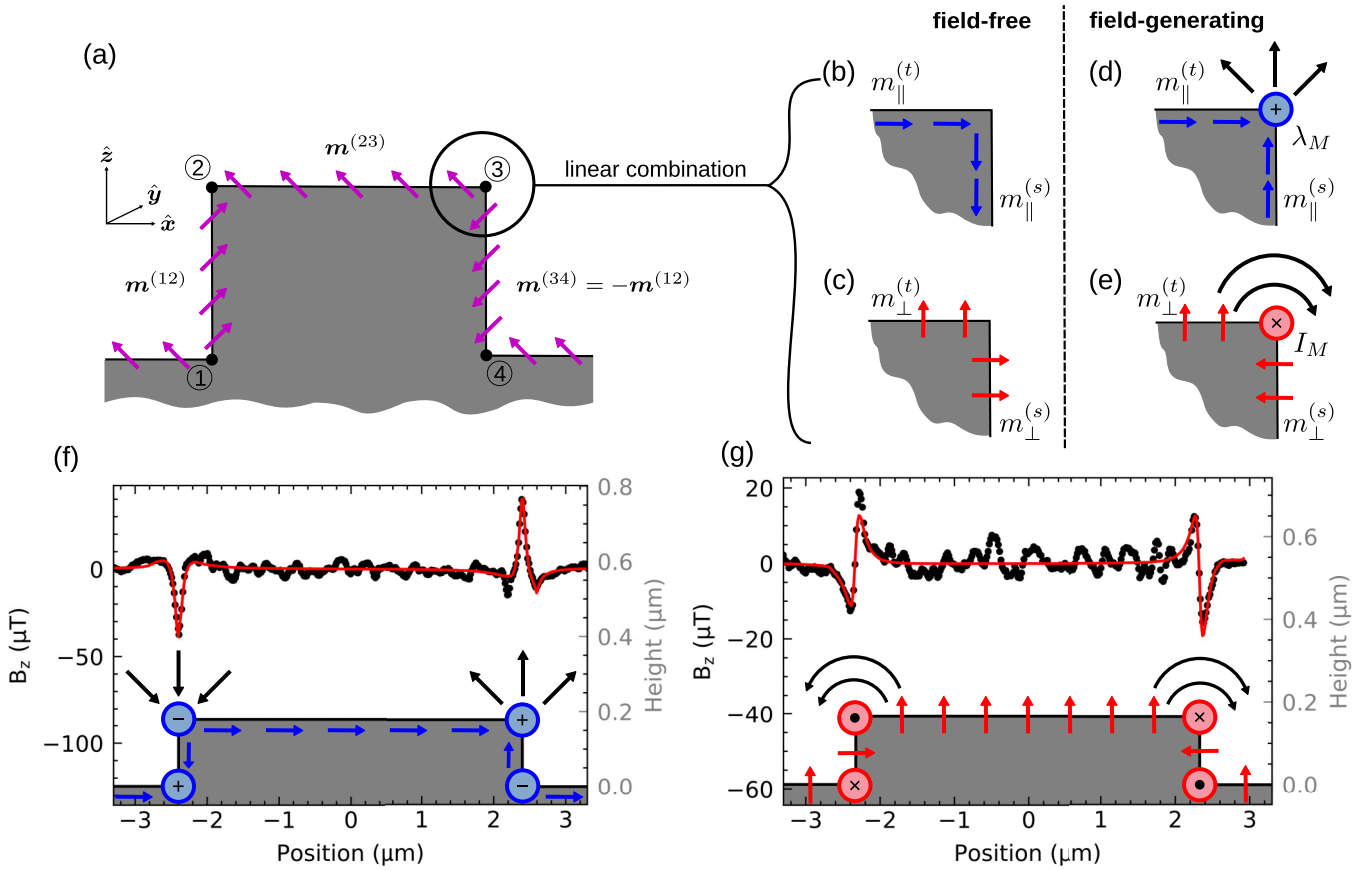


FIG. 2. Analytical model of the stray field produced by a Cr_2O_3 mesa. (a) Cross-sectional schematic of the mesa geometry used in the model, and definition of coordinate axes x, y, and z. The magnetic surface magnetizations $m^{(t,s)}$ on the top and side facets are represented by equivalent linear magnetic charge densities λ_M and currents I_M located at the mesa edges (labeled 1–4). The field detected along a scan path across the mesa corresponds to the superposition of the fields from all four edges. Illustrations of the magnetic-field patterns generated by (b) toroidal, (c) monopolar, and (d), (e) quadrupolar spin textures. Only the quadrupolar cases produce nonzero stray magnetic fields and can be addressed by SNVM. Example mesa linecuts of $\mathbf{B}_z$ [including fits of Eq. (3)] for pure charge [panel (f)] and current [panel (g)] quadrupoles. Fit parameters: $\lambda_M = 17.8 \pm 0.1$ μA, $I_M = 1.5 \pm 0.4$ μA, and $d_{\mathrm{NV}} = 58 \pm 2$ nm for panel (f) and $\lambda_M = -2.0 \pm 0.3$ μA, $I_M = -8.8 \pm 0.2$ μA, and $d_{\mathrm{NV}} = 55 \pm 2$ nm for panel (g), respectively. Insets show the current, charge, and magnetization arrangements for the two cases.

Fig. 2(a) [33]. The field of a single edge is the sum of the fields generated by λ_M and I_M, evaluated from Coulomb's law and the Biot-Savart law. A mesa linecut combines the contributions from the four mesa edges, yielding

$$\boldsymbol{B}(\boldsymbol{r}) = \frac{\mu_0}{2\pi} \sum_{i=1}^{4} \frac{(-1)^{i+1}}{R_i^2} \left(\lambda_M \boldsymbol{R}_i + I_M \begin{bmatrix} 0 & 1 \\ -1 & 0 \end{bmatrix} \boldsymbol{R}_i \right), \quad (3)$$

where the index i numerates the mesa edges as in Fig. 2(a) and $\boldsymbol{R}_i = \boldsymbol{r} - \boldsymbol{r}_i$ is the vector from edge to measurement point. Details of the NV signal and the fitting procedure are given in Appendixes D and E.

Importantly, only differences in in-plane (out-of-plane) magnetizations of adjacent facets result in nonzero values of λ_M (I_M) [see Eqs. (1)–(3) and Figs. 2(b)–2(e)], and therefore, in nonzero stray fields at mesa edges. Based on this observation, we categorize the primitive surface spin-texture combinations into the possible field-free and field-generating textures shown in Figs. 2(b)–2(e). The textures in panels (b) ("toroidal") and (c) ("monopolar") do not produce any stray fields, whereas the textures in panels (d) ("charge quadrupole") and (e) ("current quadrupole") are field generating. The quadrupolar nature [34,35] of the latter two is evident from the insets in Figs. 2(f) and 2(g), where we show example B_z linecuts, for mesas where we found $I_M = 0$ (f) or $\lambda_M = 0$, respectively. Importantly, the two cases lead to distinctly different stray-field profiles, and can therefore be properly distinguished. In general, the stray-field profile of a mesa linecut will be a linear combination of the profiles of the charge and current quadrupoles and a fit of Eq. (3) to a stray-field linecut will therefore simultaneously yield both λ_M and I_M.

III. RESULTS

To obtain a comprehensive understanding of λ_M and I_M as a function of crystal-facet orientation, we recorded stray-field linecuts on mesas with varying φ_{mesa} for both the (001)- and (104)-oriented samples. The recorded values of λ_M and I_M versus φ_{mesa} are shown in Figs. 3(a) and 3(b), and vary smoothly with φ_{mesa} for both samples [36]. On the (001)-oriented sample, both λ_M and I_M show little variation with φ_{mesa} and a behavior consistent with prior experimental studies [23,24]. Our findings that $\lambda_M \approx 0$ (specifically,

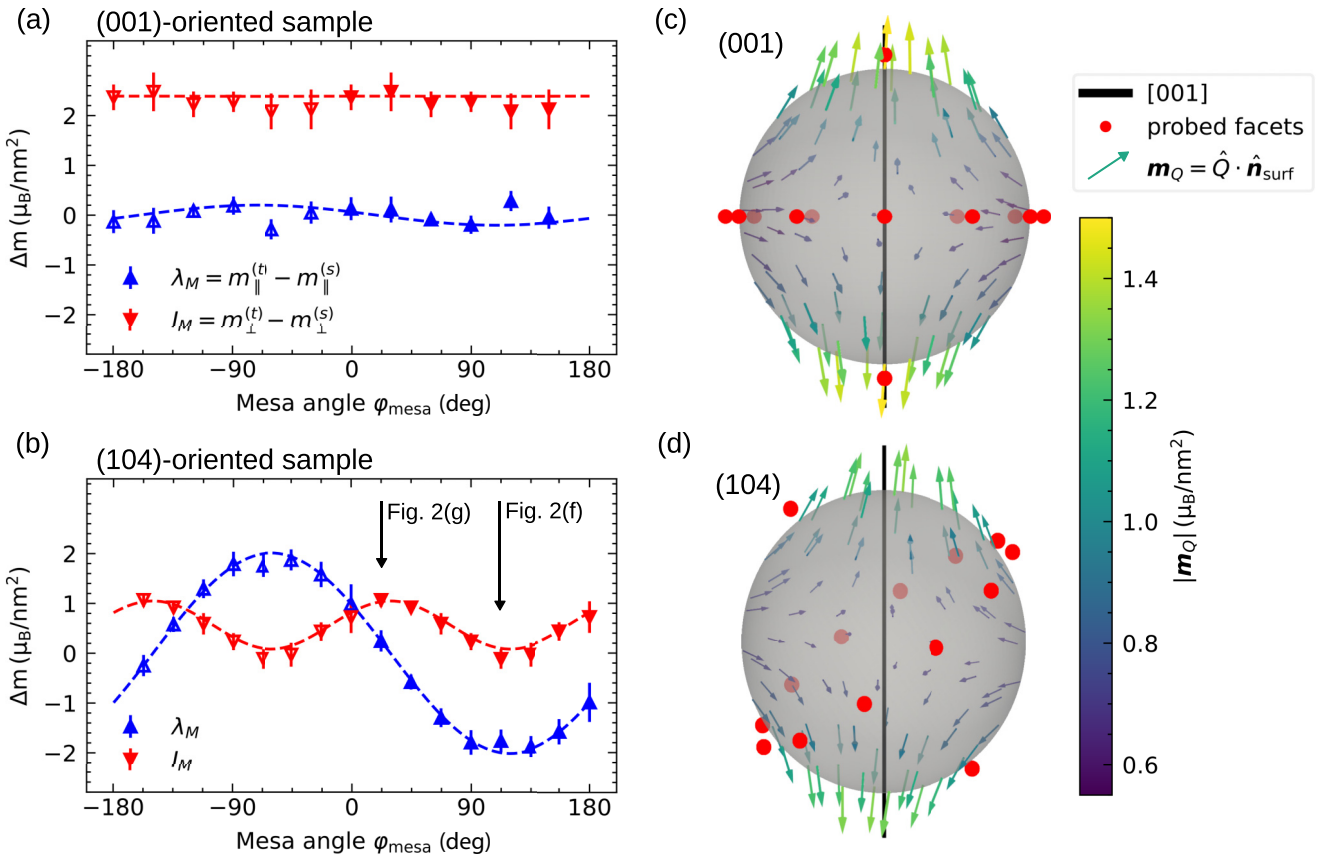


FIG. 3. Facet-dependent surface magnetization of Cr_2O_3. Extracted values of the equivalent magnetic charge densities λ_M (blue) and currents I_M (red) as a function of mesa orientation φ_{mesa} for [panel (a)] (001)- and [panel (b)] (104)-oriented crystals, where each data point results from an average of at least eight linecuts. Only data represented by full markers are independent, due to the symmetries $\lambda_M(\varphi_{\text{mesa}}) = -\lambda_M(-\varphi_{\text{mesa}})$ and $I_M(\varphi_{\text{mesa}}) = I_M(-\varphi_{\text{mesa}})$ [see Eq. (3)]. The dashed lines are fits of the magnetoelectric multipolization model [Eqs. (6) and (7)]. For the (001)-oriented sample $\lambda_M \approx 0$, while $I_M \approx 2.2\mu_B\,\text{nm}^{-2}$, consistent with literature values. For the (104)-oriented sample, both λ_M and I_M exhibit pronounced oscillations with φ_{mesa}, evidencing facet-dependent, roughness-insensitive surface magnetization of the sidewalls, including ion-plane components. (c), (d) Extension of the fitted magnetization values to the entire unit sphere. Red dots show the probed facets represented in panels (a) and (b). Despite these facets being distinct, the surface magnetization distributions for the (001)-oriented and (104)-oriented samples are similar.

$\lambda_M \leqslant 0.22\mu_B\,\text{nm}^{-2}$) indicate a purely out-of-plane surface magnetization on (001), and our fits yield $I_M = 2.39 \pm 0.2\mu_B\,\text{nm}^{-2}$, in agreement with experimental literature values for Cr_2O_3's (001) surface magnetization [22–24]. While zero-temperature calculations of the (001) surface magnetization predict $\sim 12\mu_B\,\text{nm}^{-2}$, finite-temperature simulations indicate that the outermost (001) spins become effectively paramagnetic, bringing the expected m_{surf} closer to the observed value [37]. On the (104)-oriented sample, we observe pronounced oscillation of both λ_M and I_M with φ_{mesa}, evidencing a nontrivial facet-orientation dependence of the roughness-insensitive surface magnetization in Cr_2O_3. In particular, the variation of λ_M implies a variation of $m_x^{(23)}$ and $m_z^{(34)}$ across the mesas, which constitutes facet-resolved evidence of a roughness-insensitive in-plane surface magnetization in Cr_2O_3.

So far we have related the measured stray fields to surface magnetizations on the mesa's facets. As long as pure surface effects, such as surface reconstruction, can be neglected, the surface magnetization determined in our experiments can be described as the projection of bulk multipolizations onto the surface [38,39]. We retain only the lowest order, linear term of the multipole expansion [40], such that

$$\boldsymbol{m}_{\text{surf}} = \mathcal{M} \cdot \hat{\boldsymbol{n}}. \tag{4}$$

Decomposing $\mathcal{M}$ into its irreducible components yields

$$\boldsymbol{m}_{\text{surf}} = M\,\hat{\boldsymbol{n}} + \boldsymbol{T} \times \hat{\boldsymbol{n}} + \hat{Q} \cdot \hat{\boldsymbol{n}}. \tag{5}$$

The monopolar M and toroidal $\boldsymbol{T}$ parts correspond to field-free spin-textures [see toroidal/monopolar patterns in Figs. 2(b) and 2(c)], whereas the (traceless) quadrupolar component $\hat{Q}$ generates the measurable charge- and current-quadrupole fields and is therefore directly accessible in our experiments.

For Cr_2O_3's $R\bar{3}c$ symmetry with the magnetic easy axis [001], only the diagonal elements of $\mathcal{M}$ ($\mathcal{M}_{xx} = \mathcal{M}_{yy}$ and $\mathcal{M}_{zz}$) are symmetry allowed, so the quadrupolar strength q_{z^2} is set by $(2/3) \cdot (\mathcal{M}_{zz} - \mathcal{M}_{xx})$ (see Appendix F). Consequently, within the linear description our data constrain $\mathcal{M}_{zz} - \mathcal{M}_{xx}$ together with the quadrupole orientation angles θ_c and φ_c. The

equivalent magnetic sources as a function of mesa angle are then given by (see Appendix F)

$$\lambda_M = (\mathcal{M}_{zz} - \mathcal{M}_{xx}) \cdot \sin(2\theta_c) \sin(\varphi_c - \varphi_{\text{mesa}}), \quad (6)$$

$$I_M = (\mathcal{M}_{zz} - \mathcal{M}_{xx})[\cos^2(\theta_c) - \sin^2(\theta_c)\, \sin^2(\varphi_{\text{mesa}} - \varphi_c)]. \quad (7)$$

We fit Eqs. (6) and (7) to the experimentally recorded values of λ_M and I_M [Figs. 3(a) and 3(b)] [41]. The excellent agreement between fit and data establishes a linear map that directly links each surface normal to a corresponding surface magnetization vector. This result shows that in a multipole expansion the linear term [see Eq. (4)] suffices to capture the observed stray fields of Cr_2O_3 and thereby supports the bulk-boundary correspondence predicted by the theory of multipolization for magnetoelectric antiferromagnets [17].

For both samples, the quadrupolar axes extracted through our fits align closely to the crystal's [001] direction [see Figs. 3(c) and 3(d)], which we independently determined by x-ray scattering, in line with predictions by the multipolization framework [17]. We attribute the small, $\approx 6^\circ$ misalignment from [001] we observe for the (104)-oriented sample to experimental errors related to referencing uncertainties between NV and x-ray frames. The quadrupolar strengths we determined for the two single-crystal samples amount to $q_{z^2}^{(001)} = 1.59 \pm 0.03 \mu_B\,\text{nm}^{-2}$ and $q_{z^2}^{(104)} = 1.34 \pm 0.04 \mu_B\,\text{nm}^{-2}$, respectively, where the discrepancy of these values is consistent with spreads in (001) surface magnetization values reported for different single-crystal samples in the literature [23,24]. Reasons for the discrepancy may lie in differences in the ME-annealing protocols [42] and slightly different measurement temperatures [43].

Finally, we comment on further nontrivial aspects of our findings. First, combining our results with prior work allows for a quantitative determination of the full multipolization tensor, including the monopole. For example, using $\mathcal{M}_{xx} : \mathcal{M}_{zz} = (-1) : 10$ from Ref. [20], we find $\mathcal{M}_{xx} = -0.2 \pm 0.2\,\mu_B\,\text{nm}^{-2}$ and $\mathcal{M}_{zz} = 2 \pm 0.2\,\mu_B\,\text{nm}^{-2}$, corresponding to a monopole of $a = 0.53 \pm 0.2\,\mu_B\,\text{nm}^{-2}$ and quadrupole $q_{z^2} = 1.46 \pm 0.2\,\mu_B\,\text{nm}^{-2}$. Alternatively, we find consistent results using SNVM domain-wall stray-field imaging [23,24] that directly yields the (001) surface magnetization (i.e., $\mathcal{M}_{zz}$), since domain-wall stray fields are free from any side-facet contributions. This is in agreement with theoretical predictions that, to leading order, the only nonzero element of the multipolization tensor should be $\mathcal{M}_{zz}$ [17]. Second, from our (001) dataset [Fig. 3(a)], an upper bound on the "induced" [18] surface magnetization along [001] on facets perpendicular to the (001) plane can be extracted. Such induced moments were predicted to be zero for $(\bar{1}20)$ and to be on the order of $0.1\mu_B\,\text{nm}^{-2}$ for (010) [18], and would therefore lead to a 120° oscillation in λ_M in the data shown in Fig. 3(a). A corresponding fit (see Appendix I) shows that such induced moments can be no stronger than $\approx 0.2\mu_B\,\text{nm}^{-2}$ to be consistent with our data.

Third, while we cannot formally exclude that the found surface magnetization is due to effects unrelated to the bulk structure, we deem such effects much less likely than the magnetoelectric multipolization given the quality of our samples, the close alignment of the quadrupolar axis with the crystallographic [001] direction for two samples and the consistency across multiple ME-annealing preparations (see Appendix H). In conclusion, we introduced a general method to quantify the facet-resolved surface magnetization differences of single-crystal antiferromagnets by nanoscale stray-field measurements on lithographically defined mesas. We find a linear mapping between surface magnetization and surface normal and use it to infer the bulk multipolization within the multipolization framework. Applied to Cr_2O_3, this approach yields the quadrupolar component proportional to $(\mathcal{M}_{zz} - \mathcal{M}_{xx})$, where we find consistent results across two crystals with distinct facet sets.

Our work offers a first quantitative test of the recently introduced multipolization framework for magnetoelectric AFs and the method we introduced straightforwardly translates to other AFs. A particularly noteworthy extension concerns cases where the lowest-order magnetoelectric multipolization is symmetry forbidden and only higher-order terms contribute to surface magnetization, as was predicted for FeF_2 [18]. Beyond its experimental implications, our work also provides a quantitative benchmark for *ab initio* calculations of magnetoelectric multipoles. The extracted tensor components and their facet dependence offer a direct point of comparison for recent theoretical formulations of multipolization [17,18,37], thereby establishing a unified experimental-theoretical framework for understanding bulk-surface magnetoelectric coupling in antiferromagnets.

ACKNOWLEDGMENTS

We thank Monica Schönenberger for conducting AFM measurements of mesas. This work was financially supported in part via the SERI Swiss quantum transitional call project "QuantumLeap," ERC grant 3DmultiFerro (Project No. 101141331), the European Union's Horizon 2020 research and innovation program with Grant No. 810451, and by ETH Zürich.

DATA AVAILABILITY

The data supporting the findings are available in Ref. [44]. Further information is available upon reasonable request.

APPENDIX A: CRYSTALLOGRAPHIC AND MAGNETIC STRUCTURE OF Cr_2O_3

Cr_2O_3 crystallizes in the corundum structure space group $R\bar{3}c$. The hexagonal unit cell is illustrated in Fig. 1(d). Below the Néel temperature (307 °C), the Cr ion's magnetic moments order antiferromagnetically with a pronounced uniaxial anisotropy along the crystal's [001] direction. Cr_2O_3 has two degenerate antiferromagnetic ground states. The two ground states are characterized by pairs of Cr moments pointing away from each other (OUT), as highlighted in Fig. 1(d), or toward each other (IN). Despite the absence of a net, bulk magnetic moment, the symmetry of Cr_2O_3's spin lattice is locally broken at surfaces, such that a nonzero magnetic surface magnetization may remain [16,17,45].

APPENDIX B: SAMPLE FABRICATION AND CHARACTERIZATION

Both investigated crystals were acquired commercially (MaTecK Gmbh, Jülich, Germany). The crystal structure orientation with respect to the macroscopic sample dimensions was measured using x-ray scattering. The sample's top surface was defined by polishing. The top-surface RMS roughness was measured in a commercial AFM and was found to be 2.99 and 3.26 nm, for the (001)-oriented and (104)-oriented samples, respectively. Mesa patterns were defined by *e*-beam lithography and subsequently transferred into the single crystals by reactive ion etching. The mesas on the (001)- and (104)-oriented samples were 2 and 4.7 µm wide and 80 and 170 nm high, respectively. Prior to measurements all samples were brought to a monodomain state by cooling through the Néel temperature in parallel electric and magnetic fields applied along the [001] direction and [40$\bar{1}$] direction, respectively [46,47].

APPENDIX C: SCANNING NV MAGNETOMETRY

SNVM is by now a well-established technique to measure nanoscale magnetic fields [48], electric fields [49,50], and even temperature [51]. In this technique, a single spin defect that is located at the apex of a diamond micropillar is used as a scanning probe magnetometer [52]. The NV spin is brought to a distance of about 50 nm to the sample surface and scanned over the surface, simultaneously acquiring images of the magnetic field parallel to the NV axis and the sample topography. In the field of magnetism, SNVM has been successfully applied to image AFs [53,54], ferromagnets [55], and spin waves [56]. All our scanning NV experiments were conducted at ambient conditions in a home-built confocal scanning setup. The scanning tips were partly acquired commercially (QNAMI AG, Muttenz, Switzerland) and partly fabricated in-house [22,57].

APPENDIX D: PARAMETRIZATION OF MAGNETIC FIELD PARALLEL TO THE NV

We start from Eq. (3), which we reproduce here for convenience and remind the reader that all vectors are expressed in the local mesa xz plane:

$$\begin{aligned}\boldsymbol{B}(\boldsymbol{r}) &= \frac{\mu_0}{2\pi}\sum_{i=1}^{4}\frac{(-1)^{i+1}}{R_i^2}\left(\lambda_M\boldsymbol{R}_i + I_M\begin{bmatrix}0 & 1\\ -1 & 0\end{bmatrix}\boldsymbol{R}_i\right)\\ &= \frac{\mu 0}{2\pi}\sum_{i=1}^{4}\frac{(-1)^{i+1}}{R_i^2}\begin{bmatrix}\lambda_M & I_M\\ -I_M & \lambda_M\end{bmatrix}\boldsymbol{R}_i. \qquad \text{(D1)}\end{aligned}$$

To streamline the expressions below, we reparametrize the equivalent sources as

$$\begin{bmatrix}\lambda_M\\ I_M\end{bmatrix} = A_M\begin{bmatrix}\cos\phi_M\\ \sin\phi_M\end{bmatrix}, \qquad \text{(D2)}$$

so that $A_M = \sqrt{\lambda_M^2 + I_M^2}$ and $\phi_M = \arctan(I_M/\lambda_M)$. Inserting Eq. (D2) into Eq. (D1) yields

$$\boldsymbol{B}(\boldsymbol{r}) = \frac{\mu_0 A_M}{2\pi}\sum_{i=1}^{4}\frac{(-1)^{i+1}}{R_i^2}\begin{bmatrix}\cos\phi_M & \sin\phi_M\\ -\sin\phi_M & \cos\phi_M\end{bmatrix}\boldsymbol{R}_i. \qquad \text{(D3)}$$

Hence, for each edge i, the pair $(\lambda_M,\ I_M)$ acts as a rotation by ϕ_M and a scale A_M applied to the edge-to-probe vector $\boldsymbol{R}_i$.

We next project the stray field onto the NV symmetry axis. The unit vector along the NV axis, expressed in the local mesa frame, reads

$$\hat{\boldsymbol{n}}_{\mathrm{NV}}^{\mathrm{3D}} = \begin{bmatrix}\sin(\theta_{\mathrm{NV}})\cos(\varphi_{\mathrm{NV}} - \varphi_{\mathrm{mesa}} - \pi/2)\\ \sin(\theta_{\mathrm{NV}})\sin(\varphi_{\mathrm{NV}} - \varphi_{\mathrm{mesa}} - \pi/2)\\ \cos(\theta_{\mathrm{NV}})\end{bmatrix}, \qquad \text{(D4)}$$

where $(\theta_{\mathrm{NV}}, \varphi_{\mathrm{NV}})$ are the NV's polar and azimuthal angles in the laboratory frame, and the subtraction of $\varphi_{\mathrm{mesa}} + \pi/2$ aligns the laboratory frame with the mesa coordinates (with y along the mesa's long axis). Under our assumption of invariance along y, the y component is irrelevant and we parametrize the projection of $\hat{\boldsymbol{n}}_{\mathrm{NV}}^{\mathrm{3D}}$ to the xz plane as

$$\hat{\boldsymbol{n}}_{\mathrm{NV}} = A_{\mathrm{NV}}\begin{bmatrix}\cos\phi_{\mathrm{NV}}\\ \sin\phi_{\mathrm{NV}}\end{bmatrix}, \quad |A_{\mathrm{NV}}| \leqslant 1. \qquad \text{(D5)}$$

The measured NV signal $B_{\mathrm{NV}}(\boldsymbol{r}) = \hat{\boldsymbol{n}}_{\mathrm{NV}} \cdot \boldsymbol{B}(\boldsymbol{r})$ then follows as

$$\begin{aligned}B_{\mathrm{NV}}(\boldsymbol{r}) &= \frac{\mu_0 A_M A_{\mathrm{NV}}}{2\pi}\sum_{i=1}^{4}\frac{(-1)^{i+1}}{R_i^2}\begin{bmatrix}\cos(\phi_{\mathrm{NV}} + \phi_M)\\ \sin(\phi_{\mathrm{NV}} + \phi_M)\end{bmatrix}\cdot\boldsymbol{R}_i\\ &= \frac{\mu_0 A}{2\pi}\sum_{i=1}^{4}\frac{(-1)^{i+1}}{R_i^2}\begin{bmatrix}\cos\phi\\ \sin\phi\end{bmatrix}\cdot\boldsymbol{R}_i, \qquad \text{(D6)}\end{aligned}$$

where we defined the two combinations

$$A = A_{\mathrm{NV}}A_M, \quad \phi = \phi_{\mathrm{NV}} + \phi_M.$$

Equation (D6) shows that a single linecut constrains only the composite amplitude A and angle ϕ. Consequently, extracting λ_M and I_M individually requires independent knowledge of the NV orientation.

APPENDIX E: FITTING OF MAGNETIC STRAY-FIELD LINECUTS

We fit experimental linecuts using Eq. (D6). The model contains six free parameters: the two composite quantities A and ϕ, and four geometric parameters that enter through the vectors $\boldsymbol{R}_i$, namely, the NV-sample standoff d_{NV}, mesa height, mesa width, and the mesa center position along x. The mesa height is determined independently by AFM and kept fixed during fitting. Importantly, we do not assume the NV axis *a priori* for the linecut fits; the NV orientation is only introduced later when converting the fitted $(A,\ \phi)$ into $(\lambda_M,\ I_M)$ in order to determine $\hat{Q}$.

APPENDIX F: EQUIVALENT SOURCES GENERATED BY THE QUADRUPOLAR MULTIPOLIZATION $\mathcal{M}$

Throughout this section, we use a global sample frame with $\tilde{x}$ and $\tilde{y}$ in the macroscopic top plane and $\tilde{z}$ along the top-surface normal [see Fig. 1(a)]. The mesa orientation is

specified by φ_{mesa}, the angle between the mesa's long axis (the local y axis) and the global $\tilde{x}$ axis. In our edge model, each equivalent magnetic source, λ_M and I_M, receives one contribution from the top facet and one from the adjoining side facet. We illustrate the derivation for the top-right edge [edge 3 in Fig. 2(a)], whose outward facet normals are

$$\hat{\boldsymbol{n}}_{\text{side}} = \begin{bmatrix} -\sin(\varphi_{\text{mesa}}) \\ \cos(\varphi_{\text{mesa}}) \\ 0 \end{bmatrix}, \quad \hat{\boldsymbol{n}}_{\text{top}} = \begin{bmatrix} 0 \\ 0 \\ 1 \end{bmatrix}. \tag{F1}$$

The linear magnetic charge equals the discontinuity of the in-plane magnetization across the edge,

$$\begin{aligned} \lambda_M &= \hat{\boldsymbol{n}}_{\text{side}} \cdot \boldsymbol{m}_{\text{top}} - (-\hat{\boldsymbol{n}}_{\text{top}}) \cdot \boldsymbol{m}_{\text{side}} && \text{(F2)} \\ &= \hat{\boldsymbol{n}}_{\text{side}} \cdot \mathcal{M} \cdot \hat{\boldsymbol{n}}_{\text{top}} - (-\hat{\boldsymbol{n}}_{\text{top}}) \cdot \mathcal{M} \cdot \hat{\boldsymbol{n}}_{\text{side}} && \text{(F3)} \\ &= -(\mathcal{M}_{xz} + \mathcal{M}_{zx}) \sin(\varphi_{\text{mesa}}) \\ &\quad + (\mathcal{M}_{yz} + \mathcal{M}_{zy}) \cos(\varphi_{\text{mesa}}) && \text{(F4)} \\ &= -2q_{xz} \sin(\varphi_{\text{mesa}}) + 2q_{yz} \cos(\varphi_{\text{mesa}}), && \text{(F5)} \end{aligned}$$

where on line 2 we used Eq. (4), and q_{ij} are the components of the traceless quadrupolar component $\hat{Q}$ (see, e.g., Ref. [17]). The linear magnetic current equals the difference of out-of-plane magnetization components,

$$\begin{aligned} I_M &= \hat{\boldsymbol{n}}_{\text{top}} \cdot \boldsymbol{m}_{\text{top}} - \hat{\boldsymbol{n}}_{\text{side}} \cdot \boldsymbol{m}_{\text{side}} && \text{(F6)} \\ &= \hat{\boldsymbol{n}}_{\text{top}} \cdot \mathcal{M} \cdot \hat{\boldsymbol{n}}_{\text{top}} - \hat{\boldsymbol{n}}_{\text{side}} \cdot \mathcal{M} \cdot \hat{\boldsymbol{n}}_{\text{side}} && \text{(F7)} \\ &= -\frac{\mathcal{M}_{xx}}{2} - \frac{\mathcal{M}_{yy}}{2} + \mathcal{M}_{zz} \\ &\quad + \frac{\mathcal{M}_{xx} - \mathcal{M}_{yy}}{2} \cos(2\varphi_{\text{mesa}}) \\ &\quad + \frac{\mathcal{M}_{xy} + \mathcal{M}_{yx}}{2} \sin(2\varphi_{\text{mesa}}) && \text{(F8)} \\ &= \frac{q_{x^2-y^2}}{2} \cos(2\varphi_{\text{mesa}}) + q_{xy} \sin(2\varphi_{\text{mesa}}) + \frac{3}{2} q_{z^2}, && \text{(F9)} \end{aligned}$$

with $q_{x^2-y^2}$, q_{xy}, and q_{z^2} the standard quadrupolar components of $\hat{Q}$. Neither λ_M nor I_M depends on the monopolar (trace) or toroidal (antisymmetric) components, which therefore do not produce stray fields in our geometry.

For Cr_2O_3 with $\hat{\mathbf{z}} \parallel [001]$, the symmetry-allowed form of $\mathcal{M}$ is

$$\mathcal{M}^{(001)} = \begin{bmatrix} \mathcal{M}_{xx} & 0 & 0 \\ 0 & \mathcal{M}_{xx} & 0 \\ 0 & 0 & \mathcal{M}_{zz} \end{bmatrix}$$

and the quadrupolar component

$$\hat{Q}^{(001)} = \begin{bmatrix} \frac{\mathcal{M}_{xx}-\mathcal{M}_{zz}}{3} & 0 & 0 \\ 0 & \frac{\mathcal{M}_{xx}-\mathcal{M}_{zz}}{3} & 0 \\ 0 & 0 & -\frac{2(\mathcal{M}_{xx}-\mathcal{M}_{zz})}{3} \end{bmatrix}.$$

In the general case relevant to our measurements [notably for the (104)-oriented sample], the crystallographic [001] direction ($\boldsymbol{c}$ axis) is tilted by $(\theta_c,\ \varphi_c)$ with respect to the sample frame, so that

$$\mathcal{M} = \hat{R}_z(\varphi_c)\hat{R}_y(\theta_c)\mathcal{M}^{(001)}\hat{R}_y(-\theta_c)\hat{R}_z(-\varphi_c), \tag{F10}$$

with no third rotation required because $\mathcal{M}_{xx} = \mathcal{M}_{yy}$. Substituting Eq. (F10) into Eqs. (F5)–(F9) yields the compact forms quoted in the main text,

$$\begin{aligned} \lambda_M &= (\mathcal{M}_{zz} - \mathcal{M}_{xx}) \cdot \sin(2\theta_c) \sin(\varphi_c - \varphi_{\text{mesa}}), && \text{(F11)} \\ I_M &= \frac{1}{4}(\mathcal{M}_{zz} - \mathcal{M}_{xx})[\,1 + 3\cos(2\theta_c) \\ &\quad + (1 - \cos(2\theta_c))\cos(2\varphi_{\text{mesa}} - 2\varphi_c)] && \text{(F12)} \\ &= (\mathcal{M}_{zz} - \mathcal{M}_{xx})[\cos^2(\theta_c) \\ &\quad - \sin^2(\theta_c)\ \sin^2(\varphi_{\text{mesa}} - \varphi_c)]. && \text{(F13)} \end{aligned}$$

From our measurements, we can therefore infer $q_{z^2} = 2/3(\mathcal{M}_{zz} - \mathcal{M}_{xx})$ and the angles θ_c and φ_c.

APPENDIX G: INFERENCE OF $\mathcal{M}$

From linecut fitting with Eq. (D6), we obtain the composite amplitude $A(\varphi_{\text{mesa}})$ and angle $\phi(\varphi_{\text{mesa}})$. These relate to the physical edge sources and the NV orientation via

$$A(\varphi_{\text{mesa}}) = A_{\text{NV}} \cdot \sqrt{\lambda_M^2 + I_M^2}, \tag{G1}$$

$$\phi(\varphi_{\text{mesa}}) = \phi_{\text{NV}} + \text{atan}_2(I_M, \lambda_M). \tag{G2}$$

We can then insert the explicit expressions for λ_M and I_M as well as of $\hat{\boldsymbol{n}}_{\text{NV}}$ to arrive at explicit expressions for $A(\varphi_{\text{mesa}}; q_{z^2},\ \theta_c,\ \varphi_c,\ \theta_{\text{NV}},\ \varphi_{\text{NV}})$ and $\phi(\varphi_{\text{mesa}}; q_{z^2},\ \theta_c,\ \varphi_c,\ \theta_{\text{NV}},\ \varphi_{\text{NV}})$:

$$\begin{aligned} A(\varphi_{\text{mesa}}) &= \frac{3q_{z^2}}{2}\sqrt{(\sin^2(\theta_c)\cos^2(\varphi_c - \varphi_{\text{mesa}}) - \cos^2(\theta_c))^2 + \sin^2(\theta_c)\sin^2(\varphi_c - \varphi_{\text{mesa}})} \\ &\quad \times \sqrt{\sin^2(\theta_{\text{NV}})\cos^2(\varphi_{\text{NV}} - \varphi_{\text{mesa}} - \pi/2) + \cos^2(\theta_{\text{NV}})}, && \text{(G3)} \\ \phi(\varphi_{\text{mesa}}) &= \text{atan}_2(-\sin^2(\theta_c)\cos^2(\varphi_c - \varphi_{\text{mesa}}) + \cos^2(\theta_c), \sin(\theta_c)\sin(\varphi_c - \varphi_{\text{mesa}})) \\ &\quad + \text{atan}_2(\cos(\theta_{\text{NV}}), \sin(\theta_{\text{NV}})\cos(\varphi_{\text{NV}} - \varphi_{\text{mesa}} - \pi/2)). && \text{(G4)} \end{aligned}$$

Thus, given $A(\varphi_{\text{mesa}})$ and $\phi(\varphi_{\text{mesa}})$ from Eqs. (G1) and (G2), the measured (A, ϕ) constrain the quadrupolar tensor through the unknowns $(\theta_c,\ \varphi_c,\ \mathcal{M}_{xx} - \mathcal{M}_{zz})$ together with the NV orientation $(\theta_{\text{NV}},\ \varphi_{\text{NV}})$. The NV axis is known to within $\sim 10^\circ$ from the diamond cut and bias-field alignment; in the fit, we allow $(\theta_{\text{NV}},\ \varphi_{\text{NV}})$ to vary within this bound.

We did not identify any transformations beyond inversion of the NV direction for which a different $\mathcal{M}$ would lead

TABLE I. Best-fit parameters (mean ± s.e.m.).

	(001)-oriented sample	(104)-oriented sample
θ_{NV}	$57.56 \pm 1.25^\circ$	$126.04 \pm 2.27^\circ$
φ_{NV}	$29.94 \pm 1.34^\circ$	$91.79 \pm 2.63^\circ$
θ_c	$2.55 \pm 0.95^\circ$	$43.80 \pm 1.27^\circ$
φ_c	$28.04 \pm 18.36^\circ$	$29.51 \pm 1.71^\circ$
q_{z^2}	$1.59 \pm 0.03 \mu_{\mathrm{B}}\,\mathrm{nm}^{-2}$	$1.34 \pm 0.04 \mu_{\mathrm{B}}\,\mathrm{nm}^{-2}$
$\mathcal{M}_{zz} - \mathcal{M}_{xx}$	$2.39 \pm 0.04 \mu_{\mathrm{B}}\,\mathrm{nm}^{-2}$	$2.01 \pm 0.06 \mu_{\mathrm{B}}\,\mathrm{nm}^{-2}$

to the same form of A and ϕ. Nonetheless, we performed the joined fitting of Eqs. (G1) and (G2) to $A(\varphi_{\mathrm{mesa}})$ and $\phi(\varphi_{\mathrm{mesa}})$ using NUTS sampling using the Python package pymc. This technique produces an estimate of the posterior probability distribution of the parameters given the observed data and thereby allows identification of parameter combinations, which lead to equally good fits. We do not see signs of such combinations beyond a small spread around the optimum parameters, indicating that $\mathcal{M}$ and the NV direction are well constrained by the data. The best-fit parameters (mean ± s.e.m.) are summarized in Table I.

APPENDIX H: COMPARISON OF THE TWO ANTIFERROMAGNETIC GROUND STATES ON THE (104)-ORIENTED SAMPLE

Cr_2O_3 exhibits two degenerate antiferromagnetic ground states in which the two moment pairs in the rhombohedral unit cell point either away from one another (OUT) or toward one another (IN). Monodomain preparation in either state is achieved by cooling through the Néel temperature under combined electric and magnetic fields [5,46].

We repeated the measurements on the (104)-oriented sample after preparing monodomain states using parallel and antiparallel cooling fields, respectively. Figures 4(a) and 4(b) display the extracted $\lambda_M(\varphi_{\mathrm{mesa}})$ and $I_M(\varphi_{\mathrm{mesa}})$ for both preparations; the "parallel" data coincide with those shown in Fig. 3(b). The two datasets are identical up to an overall sign,

$$\lambda_M^{(\mathrm{parallel})}(\varphi_{\mathrm{mesa}}) = -\lambda_M^{(\mathrm{antiparallel})}(\varphi_{\mathrm{mesa}}), \tag{H1}$$

$$I_M^{(\mathrm{parallel})}(\varphi_{\mathrm{mesa}}) = -I_M^{(\mathrm{antiparallel})}(\varphi_{\mathrm{mesa}}), \tag{H2}$$

within experimental uncertainty.

This behavior is the direct consequence of the linear bulk-boundary relation $\boldsymbol{m}_{\mathrm{surf}} = \mathcal{M} \cdot \hat{\mathbf{n}}$: Reversing the antiferromagnetic order parameter reverses the magnetoelectric multipolization ($\mathcal{M} \to -\mathcal{M}$), while leaving the facet normal $\hat{\mathbf{n}}$ unchanged, and therefore flips the sign of all equivalent edge sources [Eqs. (F5)–(F9)]. The magnitude and angular dependence of λ_M and I_M are otherwise preserved, confirming that the observed stray fields originate from the quadrupolar multipolization and providing an internal consistency check of the analysis across opposite antiferromagnetic domains.

APPENDIX I: INCLUDING HIGHER HARMONICS IN THE ANALYSIS OF THE (001) SAMPLE

In Eq. (4), we retained only the lowest-order term in the expansion of the surface magnetization. Allowing for higher-order contributions introduces additional harmonics in the φ_{mesa} dependence of λ_M and I_M. In particular, Ref. [18] predicts that a symmetry-allowed third-order contribution (hexadecapolization) in Cr_2O_3 would manifest as a 120°-periodic modulation for λ_M on the (001)-oriented sample. Figure 5(a) shows a fit to the (001)-oriented sample including these higher harmonics, yielding a third-harmonic component in λ_M of order $0.2\mu_{\mathrm{B}}\,\mathrm{nm}^{-2}$. In Fig. 5(b), we plot the residual after subtracting the dominant linear model contribution, leaving only the higher-order fit components. The residual fluctuations are comparable to the extracted amplitude, indicating that our signal is limited by experimental noise and/or systematic uncertainties; we therefore treat $0.2\mu_{\mathrm{B}}\,\mathrm{nm}^{-2}$ as an upper bound rather than evidence for a resolvable third-harmonic signal.

While we believe that the observations are due to errors, a varying surface magnetization on planes perpendicular to (001) would lead to such an oscillation. These surface magnetizations would be beyond a description by the magnetoelectric multipolization. We do note, however, that surface magnetizations have been found on these planes [20,21,58].

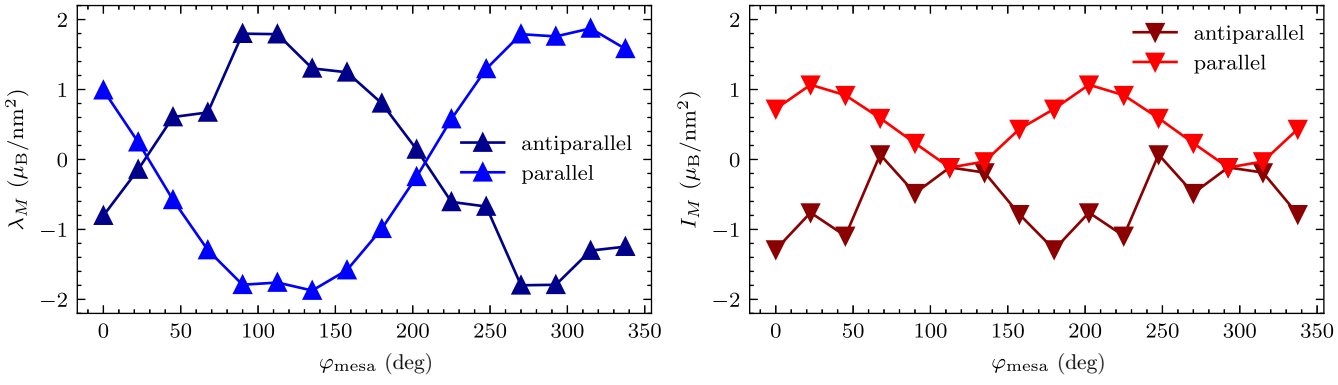


FIG. 4. Comparison of λ_M and I_M on the (104)-oriented sample prepared by ME-annealing in parallel and antiparallel $\boldsymbol{E}$ and $\boldsymbol{B}$ fields. The data for parallel annealing are the same as in Fig. 3(b).

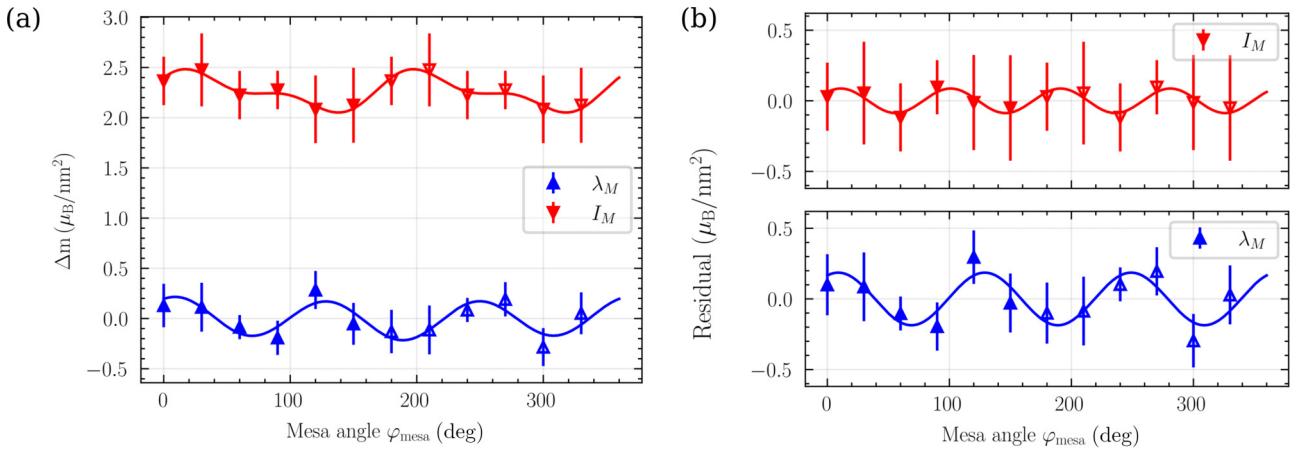


FIG. 5. Fit of the higher third order contribution to (001)-oriented sample. (a) Fit of λ_M and I_M including first and third harmonic, and constant, second and forth harmonic, respectively. (b) Residual oscillation after subtraction of the linear model fit contribution including the fitted higher-order oscillation.

[1] I. Dzyaloshinskii, On the magneto-electrical effect in antiferromagnets, J. Exp. Theor. Phys. **10**, 628 (1960).

[2] D. N. Astrov, The magnetoelectric effect in antiferromagnets, J. Exp. Theor. Phys. **11**, 708 (1960).

[3] D. N. Astrov, Magnetoelectric effect in chromium oxide, J. Exp. Theor. Phys. **13**, 729 (1961).

[4] V. J. Folen, G. T. Rado, and E. W. Stalder, Anisotropy of the magnetoelectric effect in Cr_2O_3, Phys. Rev. Lett. **6**, 607 (1961).

[5] G. T. Rado and V. J. Folen, Observation of the magnetically induced magnetoelectric effect and evidence for antiferromagnetic domains, Phys. Rev. Lett. **7**, 310 (1961).

[6] T. Jungwirth, X. Marti, P. Wadley, and J. Wunderlich, Antiferromagnetic spintronics, Nat. Nanotechnol. **11**, 231 (2016).

[7] K. Olejník, T. Seifert, Z. Kašpar, V. Novák, P. Wadley, R. P. Campion, M. Baumgartner, P. Gambardella, P. Němec, J. Wunderlich, J. Sinova, P. Kužel, M. Müller, T. Kampfrath, and T. Jungwirth, Terahertz electrical writing speed in an antiferromagnetic memory, Sci. Adv. **4**, eaar3566 (2018).

[8] J. Li, C. B. Wilson, R. Cheng, M. Lohmann, M. Kavand, W. Yuan, M. Aldosary, N. Agladze, P. Wei, M. S. Sherwin, and J. Shi, Spin current from sub-terahertz-generated antiferromagnetic magnons, Nature (London) **578**, 70 (2020).

[9] C. Binek and B. Doudin, Magnetoelectronics with magnetoelectrics, J. Phys.: Condens. Matter **17**, L39 (2005).

[10] T. Kosub, M. Kopte, F. Radu, O. G. Schmidt, and D. Makarov, All-electric access to the magnetic-field-invariant magnetization of antiferromagnets, Phys. Rev. Lett. **115**, 097201 (2015).

[11] T. Kosub, M. Kopte, R. Hühne, P. Appel, B. Shields, P. Maletinsky, R. Hübner, M. O. Liedke, J. Fassbender, O. G. Schmidt, and D. Makarov, Purely antiferromagnetic magnetoelectric random access memory, Nat. Commun. **8**, 13985 (2017).

[12] S. Manipatruni, D. E. Nikonov, C.-C. Lin, T. A. Gosavi, H. Liu, B. Prasad, Y.-L. Huang, E. Bonturim, R. Ramesh, and I. A. Young, Scalable energy-efficient magnetoelectric spin–orbit logic, Nature (London) **565**, 35 (2019).

[13] A. Mahmood, W. Echtenkamp, M. Street, J.-L. Wang, S. Cao, T. Komesu, P. A. Dowben, P. Buragohain, H. Lu, A. Gruverman, A. Parthasarathy, S. Rakheja, and C. Binek, Voltage controlled Néel vector rotation in zero magnetic field, Nat. Commun. **12**, 1674 (2021).

[14] P. Rickhaus, O. V. Pylypovskyi, G. Seniutinas, V. Borras, P. Lehmann, K. Wagner, L. Zaper, P. J. Prusik, P. Makushko, I. Veremchuk, T. Kosub, R. Hübner, D. D. Sheka, P. Maletinsky, and D. Makarov, Antiferromagnetic nanoscale bit arrays of magnetoelectric Cr_2O_3 thin films, Nano Lett. **24**, 13172 (2024).

[15] X. He, Y. Wang, N. Wu, A. N. Caruso, E. Vescovo, K. D. Belashchenko, P. A. Dowben, and C. Binek, Robust isothermal electric control of exchange bias at room temperature, Nat. Mater. **9**, 579 (2010).

[16] K. D. Belashchenko, Equilibrium magnetization at the boundary of a magnetoelectric antiferromagnet, Phys. Rev. Lett. **105**, 147204 (2010).

[17] N. A. Spaldin, Analogy between the magnetic dipole moment at the surface of a magnetoelectric and the electric charge at the surface of a ferroelectric, J. Exp. Theor. Phys. **132**, 493 (2021).

[18] S. F. Weber, A. Urru, S. Bhowal, C. Ederer, and N. A. Spaldin, Surface magnetization in antiferromagnets: Classification, example materials, and relation to magnetoelectric responses, Phys. Rev. X **14**, 021033 (2024).

[19] Although the ME-multipolization is a bulk quantity, the surface magnetization depends on the particular atomic termination at the surface.

[20] K. Du, X. Xu, C. Won, K. Wang, S. A. Crooker, S. Rangan, R. Bartynski, and S.-W. Cheong, Topological surface magnetism and Néel vector control in a magnetoelectric antiferromagnet, npj Quantum Mater. **8**, 17 (2023).

[21] O. V. Pylypovskyi, S. F. Weber, P. Makushko, I. Veremchuk, N. A. Spaldin, and D. Makarov, Surface-symmetry-driven Dzyaloshinskii-Moriya interaction and canted ferrimagnetism in collinear magnetoelectric antiferromagnet Cr_2O_3, Phys. Rev. Lett. **132**, 226702 (2024).

[22] P. Appel, B. J. Shields, T. Kosub, N. Hedrich, R. Hübner, J. Faßbender, D. Makarov, and P. Maletinsky, Nanomagnetism of magnetoelectric granular thin-film antiferromagnets, Nano Lett. **19**, 1682 (2019).

[23] N. Hedrich, K. Wagner, O. V. Pylypovskyi, B. J. Shields, T. Kosub, D. D. Sheka, D. Makarov, and P. Maletinsky, Nanoscale mechanics of antiferromagnetic domain walls, Nat. Phys. **17**, 574 (2021).

[24] M. S. Wörnle, P. Welter, M. Giraldo, T. Lottermoser, M. Fiebig, P. Gambardella, and C. L. Degen, Coexistence of Bloch and Néel walls in a collinear antiferromagnet, Phys. Rev. B **103**, 094426 (2021).

[25] P. Schoenherr, L. M. Giraldo, M. Lilienblum, M. Trassin, D. Meier, and M. Fiebig, Magnetoelectric Force Microscopy on Antiferromagnetic 180° Domains in Cr_2O_3, Materials **10**, 1051 (2017).

[26] B. B. Krichevtsov, V. V. Pavlov, R. V. Pisarev, and V. N. Gridnev, Spontaneous non-reciprocal reflection of light from antiferromagnetic Cr_2O_3, J. Phys.: Condens. Matter **5**, 8233 (1993).

[27] P. Makushko, T. Kosub, O. V. Pylypovskyi, N. Hedrich, J. Li, A. Pashkin, S. Avdoshenko, R. Hübner, F. Ganss, D. Wolf *et al.*, Flexomagnetism and vertically graded Néel temperature of antiferromagnetic Cr_2O_3 thin films, Nat. Commun. **13**, 6745 (2022).

[28] L. Rondin, J.-P. Tetienne, T. Hingant, J.-F. Roch, P. Maletinsky, and V. Jacques, Magnetometry with nitrogen-vacancy defects in diamond, Rep. Prog. Phys. **77**, 056503 (2014).

[29] A. Urru and N. A. Spaldin, Magnetic octupole tensor decomposition and second-order magnetoelectric effect, Ann. Phys. **447**, 168964 (2022).

[30] J. M. D. Coey, *Magnetism and Magnetic Materials* (Cambridge University Press, Cambridge, 2010).

[31] A. F. Andreev, Macroscopic magnetic fields of antiferromagnets, J. Exp. Theor. Phys. Lett. **63**, 758 (1996).

[32] Note that both the magnetic charge and current have units of amperes or Bohr magnetons per nanometer squared.

[33] Since we assume invariance along y, the m_y component does not contribute.

[34] D. N. Astrov, N. B. Ermakov, A. S. Borovik-Romanov, E. G. Kolevatov, and V. I. Nizhankovskii, External quadrupole magnetic field of antiferromagnetic Cr_2O_3, J. Exp. Theor. Phys. Lett. **63**, 745 (1996).

[35] A. Borovik-Romanov and V. Nizhankovskii, Quadrupolar magnetic field outside antiferromagnetic Cr_2O_3, Acta Phys. Pol. A **92**, 371 (1997).

[36] It is expected that for a particular bulk state, for different crystal facets, either of the AF's two sublattices can terminate the sample, which in turn would lead to magnetization jumps by "multipolization increments" [37]. A possible explanation for the observed smooth behavior of λ_M and I_M as a function of φ_{mesa}, could be local averaging over these two surface termination scenarios.

[37] S. F. Weber and N. A. Spaldin, Characterizing and overcoming surface paramagnetism in magnetoelectric antiferromagnets, Phys. Rev. Lett. **130**, 146701 (2023).

[38] O. L. de Lange and R. E. Raab, Electromagnetic boundary conditions in multipole theory, J. Math. Phys. **54**, 093513 (2013).

[39] W. A. Benalcazar, B. A. Bernevig, and T. L. Hughes, Electric multipole moments, topological multipole moment pumping, and chiral hinge states in crystalline insulators, Phys. Rev. B **96**, 245115 (2017).

[40] Due to the broken inversion and time-reversal symmetries, only terms odd in position are allowed for Cr_2O_3's multipole expansion.

[41] The actual fitting procedure, detailed in Appendix G, involves slightly more complicated expressions, since we also consider the NV orientation as free parameters.

[42] ME-annealing fields were applied along the [001] direction for the (001)-oriented sample and along $[\bar{4}01]$, which is normal to (104), for the (104)-oriented sample.

[43] Using literature data for the temperature dependence of Cr_2O_3's surface magnetization [20], we infer a room-temperature derivative of $\partial m_{\mathrm{surf}}/\partial T \approx -0.08\mu_{\mathrm{B}}\,\mathrm{nm}^{-2}\,\mathrm{K}^{-1}$. This implies that a temperature difference of roughly 4 K would be required to account for the observed variation in q_{z^2} between the two samples. Although sizable, such a temperature offset is plausible within our experimental setup.

[44] P. Lehmann, K. Wagner, P. Maletinsky, P. Makushko, D. Makarov, I. Veremchuk, O. Pylypovskyi, S. F. Weber, and N. Spaldin, Replication data for: Facet tomography of chromia's magnetoelectric multipole [Data set], Version 1, Zenodo, 2026, https://doi.org/10.5281/zenodo.20658751.

[45] I. Dzyaloshinskii, External magnetic fields of antiferromagnets, Solid State Commun. **82**, 579 (1992).

[46] S. Shtrikman and D. Treves, Observation of the magnetoelectric effect in Cr_2O_3 powders, Phys. Rev. **130**, 986 (1963).

[47] P. J. Brown, J. B. Forsyth, and F. Tasset, A study of magnetoelectric domain formation in Cr_2O_3, J. Phys.: Condens. Matter **10**, 663 (1998).

[48] F. Casola, T. van der Sar, and A. Yacoby, Probing condensed matter physics with magnetometry based on nitrogen-vacancy centres in diamond, Nat. Rev. Mater. **3**, 17088 (2018).

[49] W. S. Huxter, M. F. Sarott, M. Trassin, and C. L. Degen, Imaging ferroelectric domains with a single-spin scanning quantum sensor, Nat. Phys. **19**, 644 (2023).

[50] Z. Qiu, A. Hamo, U. Vool, T. X. Zhou, and A. Yacoby, Nanoscale electric field imaging with an ambient scanning quantum sensor microscope, npj Quantum Inf. **8**, 107 (2022).

[51] A. Laraoui, H. Aycock-Rizzo, Y. Gao, X. Lu, E. Riedo, and C. A. Meriles, Imaging thermal conductivity with nanoscale resolution using a scanning spin probe, Nat. Commun. **6**, 8954 (2015) 1.

[52] P. Maletinsky, S. Hong, M. S. Grinolds, B. Hausmann, M. D. Lukin, R. L. Walsworth, M. Loncar, and A. Yacoby, A robust scanning diamond sensor for nanoscale imaging with single nitrogen-vacancy centres, Nat. Nanotechnol. **7**, 320 (2012).

[53] A. K. C. Tan, H. Jani, M. Högen, L. Stefan, C. Castelnovo, D. Braund, A. Geim, A. Mechnich, M. S. G. Feuer, H. S. Knowles, A. Ariando, P. G. Radaelli, and M. Atatüre, Revealing emergent magnetic charge in an antiferromagnet with diamond quantum magnetometry, Nat. Mater. **23**, 205 (2024).

[54] A. Finco, A. Haykal, S. Fusil, P. Kumar, P. Dufour, A. Forget, D. Colson, J.-Y. Chauleau, M. Viret, N. Jaouen, V. Garcia, and V. Jacques, Imaging topological defects in a noncollinear antiferromagnet, Phys. Rev. Lett. **128**, 187201 (2022).

[55] S. K. Treves, V. Ukleev, A. Apseros, J. R. Massey, K. Wagner, P. Lehmann, A. Kitaori, N. Kanazawa, J. A. Brock, S. Finizio,

J. Reuteler, Y. Tokura, P. Maletinsky, and V. Scagnoli, Investigating skyrmion stability and core polarity reversal in $NdMn_2Ge_2$, Sci. Rep. **15**, 461 (2025).

[56] I. Bertelli, B. G. Simon, T. Yu, J. Aarts, G. E. W. Bauer, Y. M. Blanter, and T. van der Sar, Imaging spin-wave damping underneath metals using electron spins in diamond, Adv. Quantum Technol. **4**, 2100094 (2021).

[57] N. Hedrich, D. Rohner, M. Batzer, P. Maletinsky, and B. J. Shields, Parabolic diamond scanning probes for single-spin magnetic field imaging, Phys. Rev. Appl. **14**, 064007 (2020).

[58] B. Krichevtsov, V. V. Pavlov, and R. V. Pisarev, Nonreciprocal optical effects in antiferromagnetic Cr_2O_3 subjected to electric and magnetic fields, J. Exp. Theor. Phys. **67**, 378 (1988).